ELSEVIER

Journal of Wind Engineering
and Industrial Aerodynamics 93 (2005) 677–696

JOURNAL OF wind engineering AND industrial aerodynamics

www.elsevier.com/locate/jweia

Influence of floor motions in wind tunnels on the aerodynamics of road vehicles

Siniša Krajnović*, Lars Davidson

Division of Fluid Dynamics, Department of Applied Mechanics, Chalmers University of Technology, SE-412 96 Göteborg, Sweden

Received 12 September 2004; received in revised form 3 April 2005; accepted 4 May 2005
Available online 21 September 2005

Abstract

The effect of a moving floor on the flow around a simplified car with a typical fastback geometry is investigated. Two large-eddy simulations of the flows with stationary and moving floors are made and both instantaneous and time-averaged results are compared. It is found that the floor motion reduces drag by 8% and lift by 16%. Changes in the flow are found to be global but are largest close to the floor and on the rear slanted surface of the vehicle. The wake flow is found to be relatively insensitive to the floor movement, in agreement with previous experimental observations. The periodicity of the flow events is found to be dependent on whether the floor is moving. Power spectral density of both the lift and the drag contain only one dominant frequency peak when the moving floor is adopted as compared to scattered spectra in the stationary floor case. Changes in the qualitative picture of the flow are limited to the flow near the floor and on the slanted surface of the body. However, changes in the surface pressure on the body and the history of the flow show the need of a moving floor in experimental and numerical simulations.

Keywords: Road vehicle; Moving floor; Large eddy simulation; LES; Vehicle aerodynamics

*Corresponding author. Tel.: +46 31772 5272; fax: +46 3118 0976.
E-mail address: sinisa@chalmers.se (S. Krajnović).

0167-6105/$ - see front matter © 2005 Elsevier Ltd. All rights reserved.
doi:10.1016/j.jweia.2005.05.002

1. Introduction

Experimental and numerical simulations of the flows around ground vehicles strive to imitate road conditions as closely as possible. In real road conditions the road and the air are steady (apart from the air motions caused by meteorological and traffic conditions) while the vehicle is moving. Thus the floor in the experimental or virtual wind tunnel should move at the same speed as the fluid in the undisturbed part of the wind tunnel. While it is simple to obtain such a boundary condition in a numerical simulation, this is relatively difficult to achieve in an experimental study, especially in investigations of full-scale vehicles. The only practical way to ensure that there is no relative motion between the floor and the air in the experimental set-up is to use a moving belt. Several problems are related to using a moving belt. The model must be supported on a sting either from behind or above if the moving belt is employed. The sting posses the problems that it changes the flow and that, if it is not perfectly rigid, the body can move as a result of fluctuations in the flow. The moving belt must be perfectly flat and should not induce vibrations in the flow. Rotating wheels in contact with the belt will add rolling resistance to the total measured drag. Thus the wheels must be separated from the body to enable separation of the rolling resistance and the aerodynamic drag. These and some additional problems with moving belts are discussed in [1]. An alternative approach to remove relative motion between the floor and the fluid was used by Larsson et al. [2], who towed the vehicle along a water basin floor. As this approach is hardly practical for testing in the automobile industry, alternative (approximate) methods that allow the use of the stationary floors are often used. Among such methods are the use of a ground board or a porous floor with suction. The purpose of both is to reduce the boundary layer on the floor. None of these approximate methods reproduce real road conditions, and there are a number of difficulties in their application. A review of these approximate techniques is given in [1] and [3]. Furthermore, most of these methods are employed in academic research while the common approach in industry is to simply mount the vehicle on the stationary floor and to sometimes use a suction of the boundary layer upstream of the vehicle [1]. Only recently have some automotive companies started to introduce moving grounds in their wind tunnels. Exceptions are wind tunnels used for racing vehicles, where ground belts are commonly used (mainly due to the strong influence of the relative motion between the ground and a vehicle on the down-force). It is therefore important to investigate the effects of different floor boundary conditions in the wind tunnel and on the road on the flow around a vehicle and its aerodynamic properties.

One of the first investigations of the influence of the moving floor on the flow around a road vehicle was done by Bearman et al. [4], who studied flows around a typical 1:3-scale car and around a generic car shape (the so called Davis model) with stationary and moving belt floors. They measured drag and lift coefficients and found that the floor movement reduced drag by about 8% and lift by 30% for a 1:3-scale car. However, an increase in drag and reduction in lift with a moving floor was found for the Davis generic car body in [4]. The generic car bodies were equipped with an adjustable, rear-end underbody diffuser, and the influence of the floor

motions on different diffuser angles was studied. An influence of the moving floor on lift was found for diffuser angles up to 25° while drag was affected by this motion for all diffuser angles. They also found small differences in the velocity fields between moving and stationary floor conditions for the body without a diffuser.

Howell [5] used a generic car similar to the Ahmed body [6] (the main difference between the bodies in [5] and [6] is the shape of the front of the body) to study the influence of floor motion on lift and drag forces. The model was equipped with an adjustable, slanted, rear upper surface and rear-end underbody diffusers. Their experiments showed that, in comparison with a stationary floor, the moving floor produced higher drag and lower lift for almost all combinations of angles of upper slanted and diffuser surfaces. One exception is the case of a 0° diffuser and angle of the upper slanted surface of 25°. The rear-end configuration with these two angles is the subject of the present paper. It is interesting to note that they found reduced lift and no change in drag with floor motion for this case.

Lajos et al. [7] measured the flow around bus models with a moving belt and a stationary floor. The bus models had underbody up-sweep at the rear. They found a large influence on the wake flow caused by floor movements.

All the above papers considered differences between time-averaged flows between the moving and the stationary floor flows and most presented only results in the wake. Instantaneous information is becoming increasingly important in the automotive industry in the study of issues related to aerodynamics such as aeroacoustics, wind stability, and water and dirt deposition. The aim of the present paper is to investigate the influence of floor motions on both instantaneous and time-averaged flows around a generic car model.

The paper is organized as follows. The numerical method and the large eddy simulation used in the present paper are described in Section 2. The geometry of the vehicle body and the computational domain are presented in Section 3. Comparisons of the results of our LES for simulations using stationary and moving floors are given in Section 4. The instantaneous and time-averaged pressure coefficients and aerodynamic forces are discussed in Section 4.1, and a comparison of the flow structures on the slanted surface of the two flows is given in Section 4.2. The presentation of the results is concluded by a comparison of the velocities and Reynolds stresses in Section 4.3. Final remarks are given in Section 5.

2. Numerical method

Large eddy simulation (LES) has already proved to be accurate in predicting the flows around a simplified bus [8,9] and a simplified fastback model [10–13]. As LES solves the (3D) three-dimensional time-dependent Navier–Stokes equations, it is suitable for detailed studies of both instantaneous and time-averaged flows in the entire flow domain (numerical wind tunnel).

The governing LES equations are the incompressible Navier–Stokes and the continuity equations filtered with the implicit spatial filter of characteristic width, Δ

(Δ is the grid resolution in the present work):

$$\frac{\partial \bar{u}_i}{\partial t} + \frac{\partial}{\partial x_j}(\bar{u}_i \bar{u}_j) = -\frac{1}{\rho}\frac{\partial \bar{p}}{\partial x_i} + \nu \frac{\partial^2 \bar{u}_i}{\partial x_j \partial x_j} - \frac{\partial \tau_{ij}}{\partial x_j} \tag{1}$$

and

$$\frac{\partial \bar{u}_i}{\partial x_i} = 0. \tag{2}$$

Here, $\bar{u}_i$ and $\bar{p}_i$ are the resolved velocity and pressure, respectively, and the bar over the variable denotes filtering.

The influence of the small scales of the turbulence on the large energy-carrying scales in Eq. (1) is represented by the SGS stress tensor, $\tau_{ij} = \overline{u_i u_j} - \bar{u}_i \bar{u}_j$. This tensor is modeled in the present work using the Smagorinsky [14] model. This model represents the anisotropic part of the SGS stress tensor, τ_{ij}, as

$$\tau_{ij} - \frac{1}{3}\delta_{ij}\tau_{kk} = -2\nu_{\text{sgs}}\bar{S}_{ij}, \tag{3}$$

where $\nu_{\text{sgs}} = (C_s f \Delta)^2 \, |\bar{S}|$ is the SGS viscosity,

$$\bar{S}_{ij} = \frac{1}{2}\left(\frac{\partial \bar{u}_i}{\partial x_j} + \frac{\partial \bar{u}_j}{\partial x_i}\right) \tag{4}$$

is the resolved rate-of-strain tensor and $|\bar{S}| = (2\bar{S}_{ij}\bar{S}_{ij})^{1/2}$. f in the expression for the SGS viscosity is the van Driest damping function

$$f = 1 - \exp\left(\frac{y^+}{25}\right). \tag{5}$$

Here, the value of the Smagorinsky constant, C_s, is 0.1.

Eqs. (1) and (2) are discretized using a 3D finite volume method for solving the incompressible Navier–Stokes equations with a collocated grid arrangement [15]. Both convective and viscous plus sub-grid fluxes are approximated by central differences of second-order accuracy. The time integration is done using the second-order Crank–Nicolson scheme. Although no explicit dissipation is added to prevent odd-even decoupling, an implicit dissipation is present. This is done by adding the difference between the pressure gradient at the face and the node. It can be shown that this term is proportional to the third derivative of pressure, i.e. $\partial^3 p/\partial x_i^3$. This term corresponds to Rhie–Chow dissipation [16]. The SIMPLEC algorithm is used for the pressure-velocity coupling. The code is parallelized using block decomposition and the MPI message passing system [17].

3. Generic vehicle body

As mentioned, the flow around a simplified fastback model was accurately predicted using LES in Refs. [10–13]. This model is well known as the Ahmed body and measurements on it are available in Ahmed et al. [6] and Lienhart and Becker

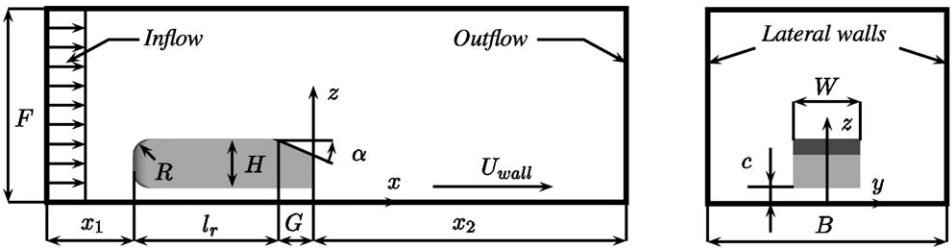

Fig. 1. Schematic representation of the computational domain with vehicle body. $U_{wall} = U_\infty$ and $U_{wall} = 0$ when the floor is moving and stationary, respectively. Left: view from the side; right: view from behind the body.

[18]. The geometry of the body and the computational domain are given in Fig. 1. The main feature of this body is the surface of the rear window, which is slanted with respect to the horizontal surface of the roof of the body. In the present paper the angle of the slant, α, is chosen to be 25° (thus the same as in [10–13]). All the geometric quantities are normalized with the body height, H, which is 0.288 m. The values of the geometric quantities are $l_r/H = 2.928$, $G/H = 0.697$ and $W/H = 1.35$. The front part is rounded with a radius of $R/H = 0.347$ in symmetry planes $y = 0$ and $z = 0$. The geometry of the rounded corners is made from the data (in the form of distinct points) measured at the body used in Ahmed et al. [6] and Lienhart and Becker [18].

This body is placed in a channel with a cross section of $B \times F = 6.493H \times 4.861H$ (width × height). The cross section of this channel is identical to the open test section of the wind tunnel used in the experiments of Lienhart and Becker [18]. The front face of the body is located at a distance of $x_1 = 7.3H$ from the channel inlet, and the downstream length between the rear face of the body and the channel outlet is $x_2 = 21H$. The body is raised from the floor to produce a ground clearance of $c/H = 0.174$, which is the same as in the experiments. The Reynolds number of 7.68×10^5, based on the incoming velocity U_∞ and the car height H, that was used in the experiments [18] is reduced here to $Re = 2 \times 10^5$.

A uniform velocity profile, U_∞, constant in time is used as the inlet boundary condition. The convective boundary condition of $\partial\bar{u}_i/\partial t + U_\infty(\partial\bar{u}_i/\partial x) = 0$ is used at the downstream boundary. The lateral surfaces and the ceiling are treated as slip surfaces using symmetry conditions ($\partial\bar{u}/\partial y = \partial\bar{w}/\partial y = \bar{v} = 0$ for the lateral sides and $\partial\bar{u}/\partial z = \partial\bar{v}/\partial z = \bar{w} = 0$ for the ceiling). This boundary condition is different from the open jet tunnel, where no lateral sides or ceiling exist. The consequence of this boundary condition is that the flow across the lateral sides and the ceiling is permitted in the experiment but not in the simulation, which results in different effective blocking of the cross section. However, we used the same boundary conditions for the lateral surfaces and the ceiling in both our simulations, i.e. with the moving and the stationary floor. Thus the study of the floor motions on the flow is not influenced by the difference in the boundary conditions between the experimental and the numerical set-ups. No-slip boundary conditions are used on the surface of the body. The instantaneous wall functions based on the log-law (see

[9] for details) and the velocity equal to the velocity at the inlet, U_∞, are applied on the channel floor in the case of the stationary and moving floors, respectively.

Numerical accuracy is established by making three LES on different computational grids containing 3.5, 9.6 and 16.5 million nodes (see [10–13]). In this paper we present results for the fine mesh only. The time step is 1×10^{-4}, giving a maximum CFL number of approximately 0.9. The averaging time, tU_∞/H, in the simulations is 38.2 (110,000 time steps).

4. Results

As the flow enters the underbody region, a boundary layer is formed on the underbody surface. The boundary layer retards the flow close to the walls in the streamwise direction. The flow outside the boundary layer between the underbody and the floor does not want to accelerate and, in order to fulfill continuity, flow moves in the lateral directions. In the case of the stationary floor an additional boundary layer is formed on the floor of the wind tunnel. The consequence of the boundary layer on the floor is a stronger retardation of the flow in the streamwise direction in the case of the stationary floor. To study the influence of the moving floor on the flow underneath the body, we computed the mass flux under the body in the streamwise and spanwise directions. As can be seen in Fig. 2a the moving floor case has between 5% and 11% more mass flux in the streamwise direction at positions $x/H = -3.26$ and $x/H = 0$, respectively. Consistent with the continuity equation, the mass flux in the spanwise direction is larger in the stationary floor case (see Fig. 2b). The difference between the two fluxes increases from the symmetry plane toward the lateral side of the body, where it is approximately 13%. We expect

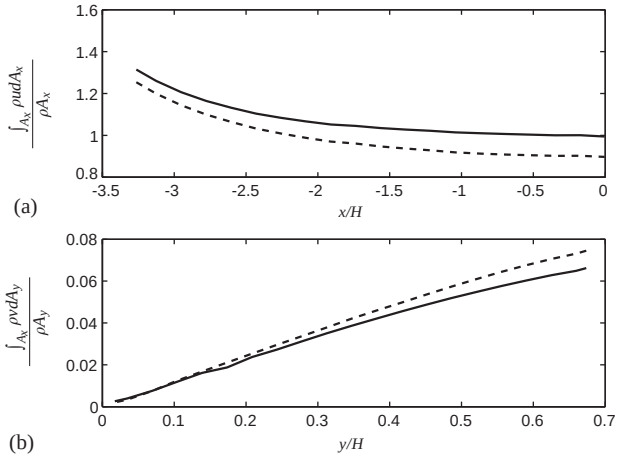

Fig. 2. The mass flux integrated under the body across (a) x planes; (b) y planes. Moving floor (solid line), stationary floor (dashed line).

that these differences in the mass fluxes will have implications for the flow structures and the resulting aerodynamic forces.

4.1. Aerodynamic forces

The relative motion of the floor with respect to the vehicle affects the aerodynamic forces. The studies reported in [4,5] showed that it is not possible to draw general conclusions on changes in the drag and lift depending on floor movements as these depend on a number of factors such as ground clearance and body shape. The body studied in the present paper is characterized by a rear slant angle of 25°, which was also used in [5]. The geometry of the fronts of the bodies in [5] and in the present paper are different, however. Our goal was to study the differences both in the instantaneous and the time-averaged forces between the moving and the stationary floor flows.

The time history of the drag and the lift coefficients for both cases are thus computed as $C_D = D/0.5\rho U_\infty^2 A$ and $C_L = L/0.5\rho U_\infty^2 A$, respectively. Here ρ is density, D and L are drag and lift forces due to the pressure, respectively, and A is the frontal area. Note that the reference area for both coefficients is the same projected frontal area. The time histories of these force coefficients are shown in Figs. 3 and 4. These are used to compute the mean and the r.m.s. values presented in Table 1. It can be seen that the motion of the floor reduced the drag by some 8% and lift by 16%. $C_{D_{RMS}}$ and $C_{L_{RMS}}$ are unchanged. Another interesting observaton is that the C_L signal is cleaner (without overlapping noise) when the moving floor is employed, see Fig. 4. The high frequency noise in the C_L signal with the stationary floor is probably caused by the interaction of the instantaneous boundary layer underneath the body with that on the stationary floor.

The time histories of the integrated pressure coefficients were Fourier transformed and the dominant frequencies identified. The energy of the C_L signal is concentrated around the non-dimensional frequency of $St = 0.5$ (see Fig. 5a) in the case of the moving floor. The same energy is divided between four motions of different

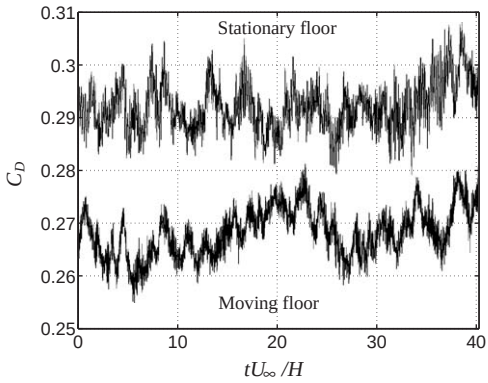

Fig. 3. Time history of the drag coefficient.

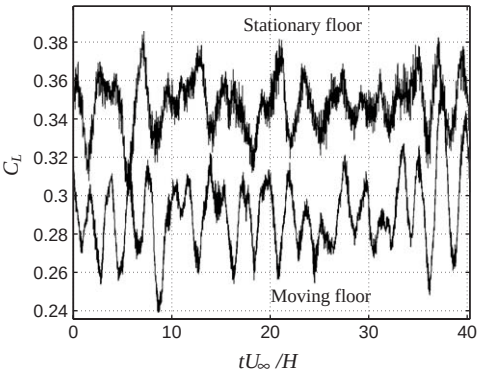

Fig. 4. Time history of the lift coefficient.

Table 1
Time-averaged pressure drag ($\langle C_D \rangle_t$) and lift ($\langle C_L \rangle_t$) coefficients

Case	$\langle C_D \rangle_t$	$C_{D_{RMS}}$	$\langle C_L \rangle_t$	$C_{L_{RMS}}$	$\langle C_{D_S} \rangle_t$	$C_{D_{S_{RMS}}}$	$\langle C_{D_B} \rangle_t$	$C_{D_{B_{RMS}}}$
Moving floor	0.269	0.005	0.290	0.020	0.185	0.003	0.073	0.002
Stationary floor	0.292	0.005	0.344	0.020	0.204	0.003	0.088	0.002

Time-averaged contribution of the rear slanted and rear vertical surfaces to the total pressure drag, $\langle C_{D_S} \rangle_t$ and $\langle C_{D_B} \rangle_t$, respectively. The r.m.s. values are denoted with the subscript RMS (such as $C_{D_{RMS}}$ in the r.m.s. value of the drag coefficient).

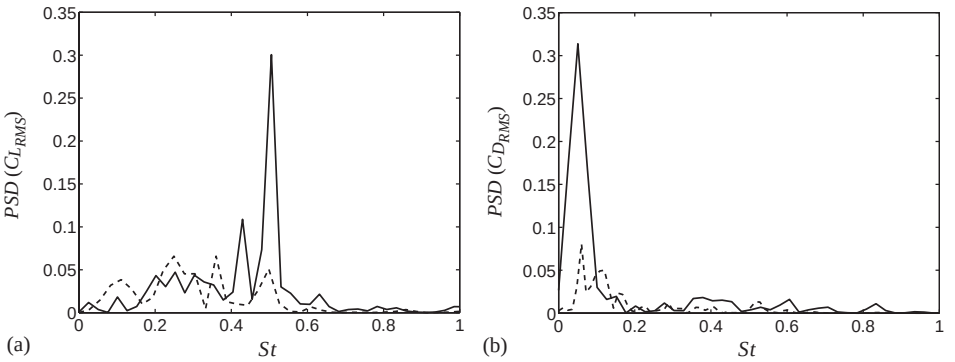

Fig. 5. Power spectral density of (a) the lift, C_L, and (b) the drag coefficients, C_D. Spectrum of the moving floor is drawn with solid line and that of the stationary floor with the dashed line.

periodicity in the case of the stationary floor (see Fig. 5a). Although the peak at $St = 0.5$ persists here, it contains about six times less energy than in the case of the moving floor. A similar situation is observed for the drag coefficient spectrum, where the energy is concentrated around the frequency of $St = 0.05$ in the case of the

moving floor (see Fig. 5b). The energy of the drag coefficient is more scattered when the floor is stationary (see Fig. 5b). A peak was also found here at $St = 0.05$ but had one fourth the amplitude of that in the moving floor case.

As mentioned above the oscillations of the lift force coefficient are more distinct when the floor is moving than in the case of the stationary floor. To understand the processes that govern this regular increase and decrease in the lift, we visualize the flow structures at the minimum and maximum C_L values in Figs. 6 and 7, respectively. The chief difference between the two pictures is the existence of a strong spanwise vortex in the wake close to the floor at low lift. As this vortex breaks down in Fig. 7, a high pressure region is formed on the underbody close to the rear of the body (not visible in Fig. 7) that continues onto the rear vertical surface (see region HP) in Fig. 7. These regions of high pressure are responsible for the major part of the increase in the lift coefficient. It is also found that the surface pressure on the slanted surface is higher in Fig. 6 than in Fig. 7, further decreasing the lift here (note the existence of the high pressure spots *HS* on the slanted surface in Fig. 6 and their absence in Fig. 7).

In addition to computing the lift and the drag coefficients, we have also integrated the streamwise component of the pressure force coefficients for the rear slanted and the rear vertical surfaces (see Fig. 8). The same peak at $St = 0.05$ as in the power spectral density of C_D in the moving floor case is found in the C_S signal, see Fig. 9b. Thus the strong periodicity of the drag coefficient is defined by the pressure oscillations on the slanted surface. The dominant frequency of $St = 0.021$ is found in the C_B signal in the moving floor case. Table 1 shows contributions of the rear slanted and the rear vertical surfaces to the total pressure drag (C_{D_S} and C_{D_B},

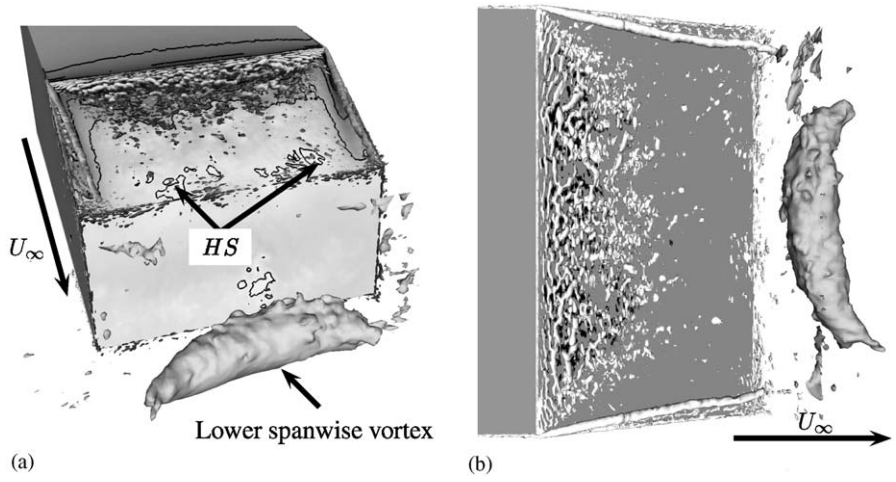

Fig. 6. Snapshot of a low value of C_L. Moving floor. Isosurfaces of the pressure, $p = -0.2$, and the second invariant of the velocity gradient, $Q = 7000$. Both the color and the isocurves on the body are of the surface pressure. (a) View from behind the body. (b) View from above. The white vortices on the slanted surface in the view from above are traveling downstream and black vortices are traveling upstream.

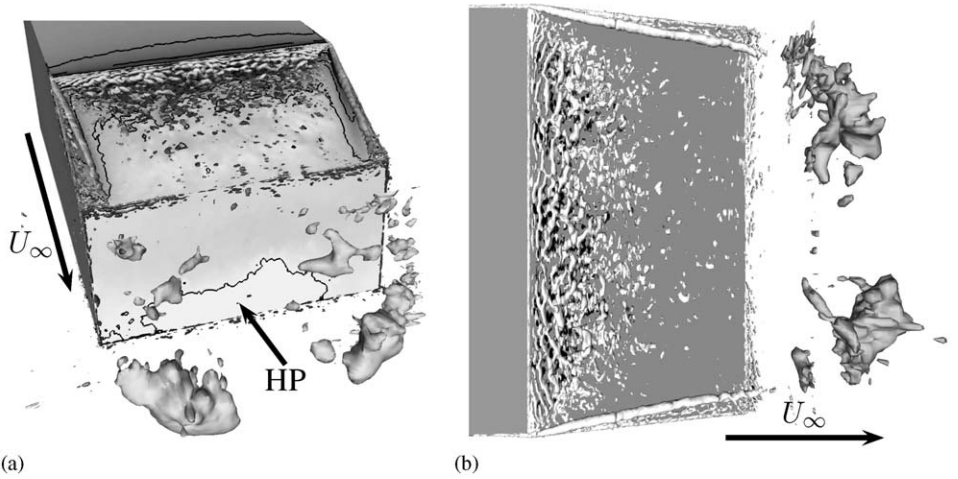

Fig. 7. Snapshot of a high value of C_L. Moving floor. Isosurfaces of the pressure, $p = -0.2$, and the second invariant of the velocity gradient, $Q = 7000$. Both the color and the isocurves on the body are of the surface pressure. (a) View from behind the body. (b) View from above.

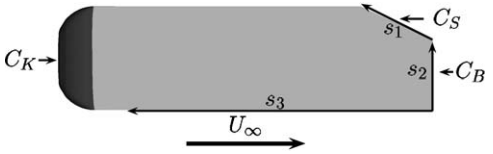

Fig. 8. Schematic representation of the pressure drag breakdown. C_K, C_S and C_B are the streamwise components of the pressure force coefficients from the front, the rear slanted and the rear vertical surfaces, respectively.

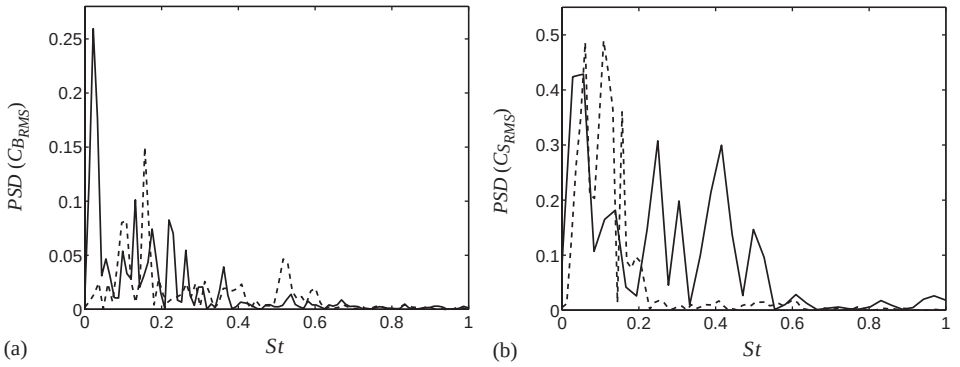

Fig. 9. Power spectral density of (a) C_B and (b) C_S. Spectrum of the moving floor is drawn with the solid line and that of the stationary floor with the dashed line.

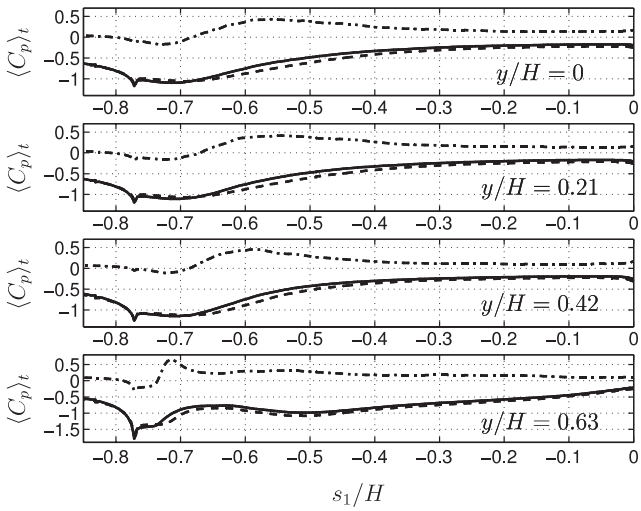

Fig. 10. Distribution of the time-averaged surface pressure coefficients along the slanted surface in planes: $y = 0$, $y = 0.21H$, $y = 0.42H$ and $y = 0.63H$. Moving floor (solid curve); stationary floor (dashed curve); 3× difference between moving and stationery floor (dashed–dotted curve).

respectively). The mean values of C_{D_S} and C_{D_B} decrease by some 10% and 17%, respectively, when the moving floor is employed (see Table 1). The r.m.s. values of both C_{D_S} and C_{D_B} remain unchanged.

The surface pressure coefficients are computed along the slanted, rear vertical and underbody surfaces, as shown in Fig. 8, and plotted for planes $y/H = 0$, 0.21, 0.42 and 0.63 in Figs. 10–12. Let us consider the surface pressure profiles on the slanted surface in Fig. 10. For positions $y/H = 0$, 0.21 and 0.42, the stationary floor case has a lower pressure between approximately $s_1/H = -0.69$ and $s_1/H = 0$ and a higher pressure between $s_1/H = -0.79$ and $s_1/H = -0.69$. The largest difference occurs at $s_1/H = -0.55$ for $y/H = 0$ and $y/H = 0.21$ and at $s_1/H = -0.6$ for $y/H = 0.42$. The differences between the two cases in $\langle C_p \rangle_t$ close to the lateral edge are different from those in three other planes (see plane $y/H = 0.63$ in Fig. 10). Here the stationery floor case has a lower pressure at all positions except between $s_1/H = -0.78$ and $s_1/H = -0.74$ (the region close to the pressure dip after the separation at the sharp edge).

Profiles of $\langle C_p \rangle_t$ along the rear vertical surface are shown in Fig. 11 for $y/H = 0$, 0.21, 0.42 and 0.63 from left to right. Again the stationary floor case has a lower pressure coefficient than that in the moving floor case. The greatest difference can be found in the symmetry plane. This difference decreases toward the lateral side of the body, and the two profiles are closest at position $y/H = 0.42$. The difference in $\langle C_p \rangle_t$ increases again very close to the lateral edge.

Finally, let us consider the surface pressure coefficients along the underbody in Fig. 12. Although the $\langle C_p \rangle_t$ in the stationary floor case is higher close to the front of the body (up to $s_3/H = -2.5$ in the symmetry plane $y/H = 0$) it is lower along the

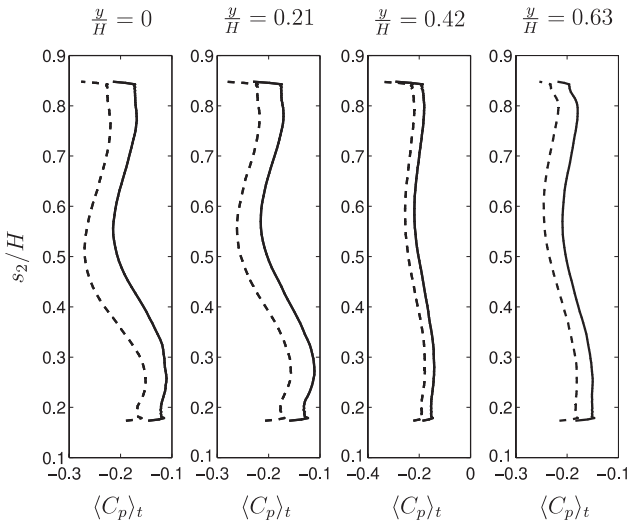

Fig. 11. Distribution of the time-averaged surface pressure coefficients along the rear vertical surface in planes: $y = 0$, $y = 0.21H$, $y = 0.42H$ and $y = 0.63H$ from left to right. Moving floor (solid curve); stationary floor (dashed curve).

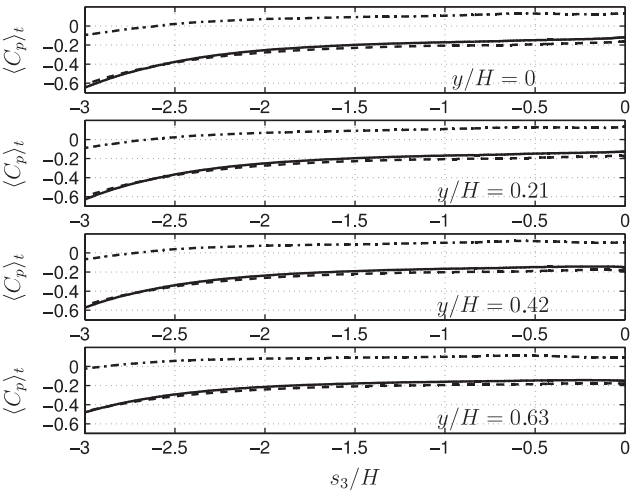

Fig. 12. Distribution of the time-averaged surface pressure coefficients along the underbody in planes: $y = 0$, $y = 0.21H$, $y = 0.42H$ and $y = 0.63H$. Moving floor (solid curve); stationary floor (dashed curve); 3× difference between moving and stationary floor (dashed–dotted curve).

rest of the underbody all the way to the rear of the body. This difference increases toward the rear of the body and in the symmetry plane, for example, the stationary floor case has a 37% lower $\langle C_p \rangle_t$ at the rear edge ($s_3/H = 0$) than the moving floor case.

4.2. Structures on the slanted surface

As the Navier–Stokes equations governing the flow are elliptic, the change in the boundary condition on the floor has a global influence on the flow. Therefore we not only studied changes in the flow features close to the floor but also in other regions, such as on the slanted surface. Although the imprints of the vortices on the slanted surface appear to be identical at first sight, there are differences in the size of the spanwise vortex, V_{SL} (see Fig. 13). The extension of this vortex decreases from $X_{SL2} = 0.35H$ to $X_{SL1} = 0.29H$ when the floor is moving. A thinner vortex, V_{SL}, in the case of the moving floor implies a smaller region of low pressure below it and thus higher pressure on the slanted surface. This contributes to the lower lift coefficients when the floor is moving. We have seen in Fig. 12 that the underbody pressure is higher when the floor is moving, thus contributing to the higher lift. The contribution of the surface pressure from the slanted surface dominates the lift, however, resulting in lower lift when the floor is moving. No significant influence of the moving floor on cone-like vortices $T_{\ell 3}$ and T_{r3} close to the lateral edges, S_ℓ, is observed (see Fig. 13).

Let us now look in more detail at one part of this flow in Fig. 14, namely regions A and B from Fig. 13. The focus, P_b, found in the base of the vortex, V_{SL}, in the flow with the stationary floor is not found when the floor is moving (see Fig. 14). Instead an unstable node, N_b, is found here. The flows on the slanted surface are symmetrical around plane $y = 0$ (Fig. 13) and corresponding focus and node exist on the right side of the slanted surface.

4.3. Comparison of the velocities and Reynolds stresses

In this section we present comparisons of the profiles for velocities and Reynolds stresses in three planes, $y = 0$, $y = 0.35H$ and $y = 0.63H$. These planes are chosen because the experimental data by Lienhart and Becker [18] exist for these three planes and our LES have already shown good agreement (for the stationary floor case) with the experimental data in these planes in [10–12]. In [10–12] we compared velocities and stresses in our LES results and the experimental data. The results of the LES calculation using a fine computational mesh (around 16.5 million nodes)

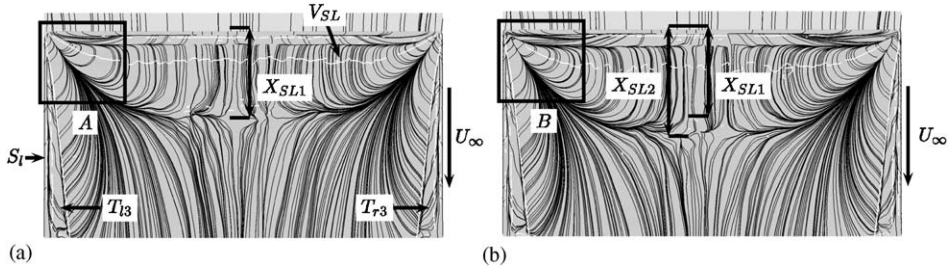

Fig. 13. Time-averaged trace lines on the rear slanted surface of the body. View from above of the lateral surface of the body. Vortex cores are denoted with white curves. (a) Moving floor. (b) Stationary floor.

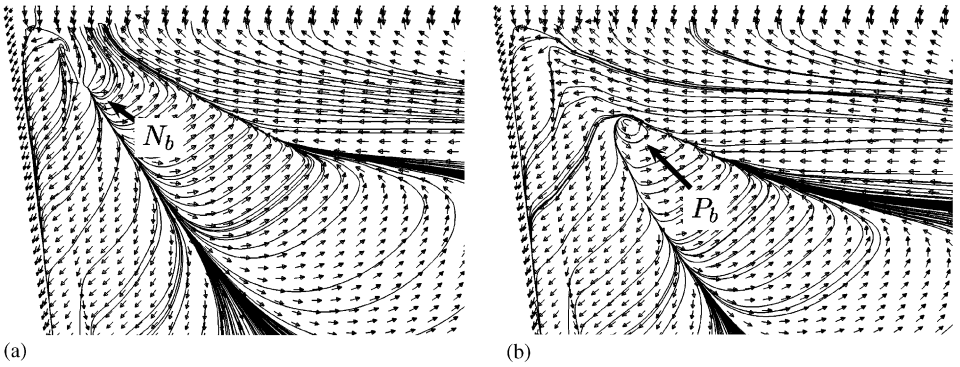

Fig. 14. Zoom of regions A and B from Fig. 13. Velocity vectors are plotted in the first computational nodes above the surface of the body. (a) Moving floor. (b) Stationary floor.

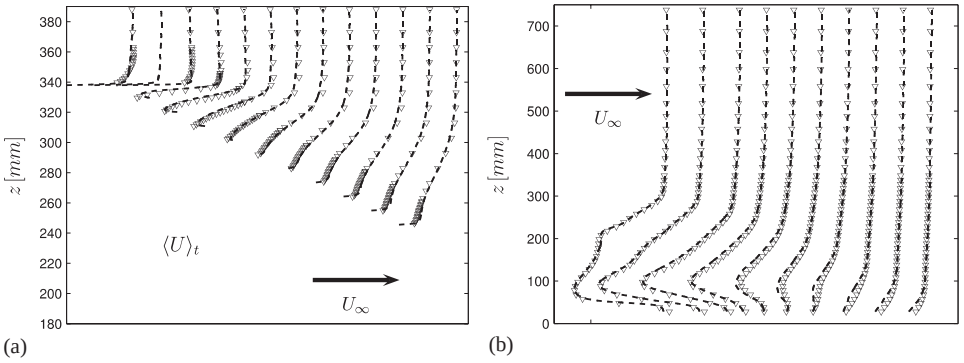

Fig. 15. Comparison of the time-averaged $\langle U \rangle_t$ velocity profiles in the symmetry plane ($y = 0$) in simulation using the stationary floor: (a) Slanted surface; (b) wake region. LES (dashed curve); experiments (symbols).

were in perfect agreement with the experimental data at almost all positions on the slant and in the near wake (see for example Fig. 15).

Comparisons of velocity profiles $\langle U \rangle_t$ and $\langle W \rangle_t$ in plane $y = 0$ are shown in Fig. 16. Fig. 16a presents streamwise velocity profiles, $\langle U \rangle_t$, on the roof and the slanted surface for positions between $x = -0.844H$ and $x = -0.01H$ (from left to right), where the space difference between the two profiles is $\Delta x = 0.07H$. The stationary floor case has smaller streamwise velocities between positions $x = -0.635H$ (the fourth profile from the left) and the profile close to the rear end of the body ($x = -0.01H$). These differences are found up to approximately $z = 340$ mm. In addition, the moving floor profile at $x = -0.427H$ (the seventh profile from the left) is almost completely positive, showing that flow has already re-attached. In comparison, the stationary floor flow is still separated and it is shown to be re-attached first at the next position ($x = -0.358H$). This is in agreement with our

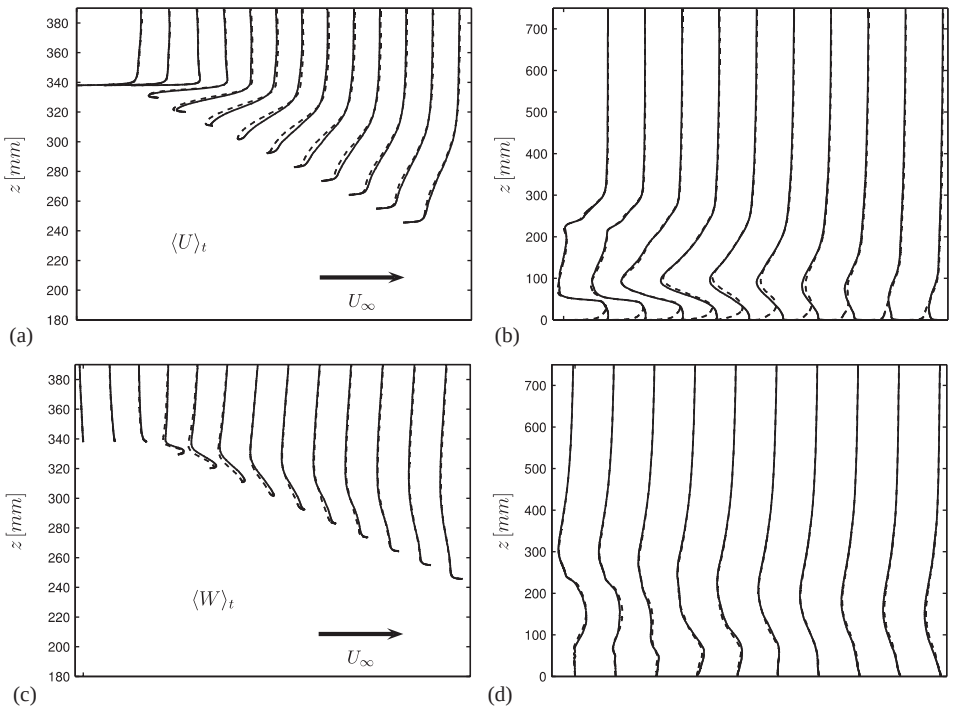

Fig. 16. Time-averaged $\langle U\rangle_t$ (Figs. (a) and (b)) and $\langle W\rangle_t$ (Figs. (c) and (d)) velocity profiles in the symmetry plane ($y = 0$). Left: slanted surface; right: wake region. Moving floor (solid curve). Stationary floor (dashed curve).

observation of the shorter re-attachment length in the moving floor flow in the previous section.

Fig. 16c shows velocity profiles $\langle W\rangle_t$ on the slanted surface. Similar to the $\langle U\rangle_t$ velocities, the $\langle W\rangle_t$ profiles from the stationary floor case have a lower magnitude downstream of position $x = -0.635H$ (the fourth profile from the left).

Let us now consider the flow in the wake. Figs. 16(b) and (d) present $\langle U\rangle_t$ and $\langle W\rangle_t$ velocity profiles in the wake region behind the body for positions x equal to $0.059H$, $0.132H$, $0.306H$, $0.479H$, $0.653H$, $0.826H$, H, $1.174H$, $1.521H$, $1.868H$ and $2.215H$, from left to right. As the floor boundary condition is different in the two cases, the $\langle U\rangle_t$ profiles are different up to approximately $z = 50$ mm (see Fig. 16b), i.e. the height of the shear layer from the underbody. We can also see that the moving floor case profiles (between approximately $z = 50$ and 120 mm) are slightly lower between $x = 0.479H$ (the fourth profile from the left) and $x = 1.521H$ (the eighth profile from the left). There are no significant differences in the $\langle W\rangle_t$ velocity profiles in the wake between the stationary and the moving floor case (see Fig. 16d).

Reynolds stresses are compared in Fig. 17. There are almost no differences in the normal stresses, $\langle uu\rangle_t$ (see Fig. 17a) and $\langle ww\rangle_t$ (not shown here), on the slanted surface. Some differences are observed in the shear stresses, $\langle uw\rangle_t$, in Fig. 17c

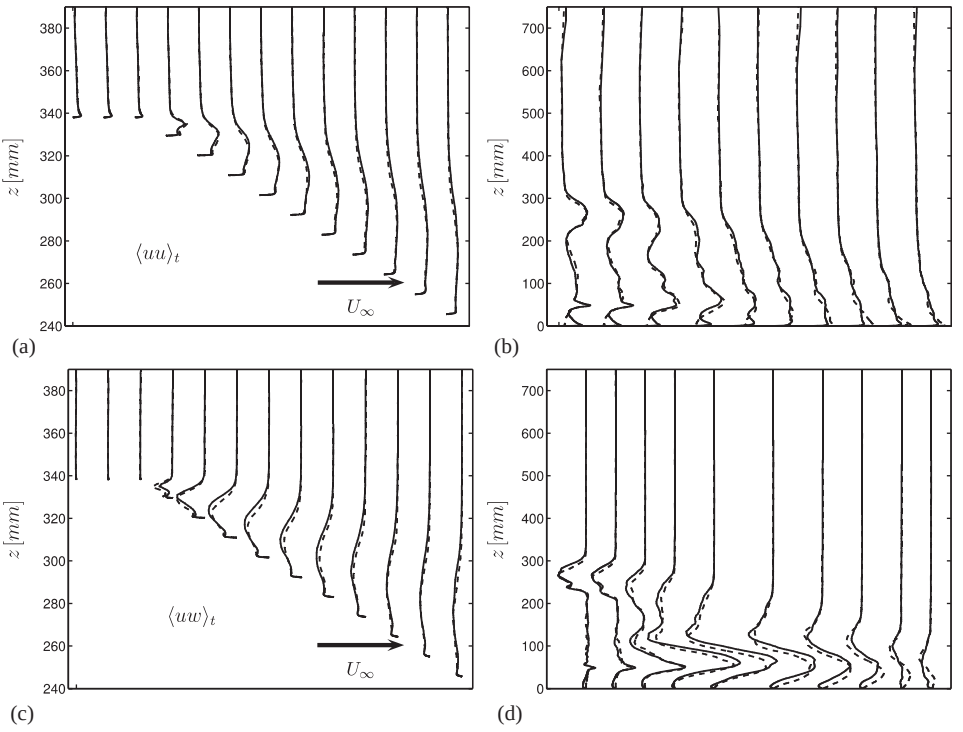

Fig. 17. Time-averaged Reynolds stresses in the symmetry plane ($y = 0$). $\langle uu\rangle_t$ (Figs. (a) and (b)); $\langle uw\rangle_t$ (Figs. (c) and (d)). Left: slanted surface; right: wake region. Moving floor (solid curve). Stationary floor (dashed curve).

between positions after the separation on the sharp edge at $x = -0.635H$ (the fourth profile from the left) and $x = -0.219H$ (the tenth profile from the left).

The wake flow below the shear layer coming from the underbody (for approximately $z < 50$ mm) is more turbulent downstream of the body up to $0.653H$ (the fifth profile from the left) when the floor is moving (see Fig. 17b). The magnitudes of $\langle uu\rangle_t$ below $z < 50$ mm for the moving and the stationary floors are approximately equal at $0.826H$ (the sixth profile from the left), to go in favor of the stationary floor after that position.

Differences in the shear stresses $\langle uw\rangle_t$ in the wake can be divided into two parts (Fig. 17d). The first contains the flow coming from the slanted surface (profiles $x = 0.059H$–$0.653H$ between $z = 150$ and 300 mm). The magnitude of $\langle uw\rangle_t$ is decreased in this region when the floor is moving. The second region is located downstream of $x = 0.479H$ (the fourth profile from the left) and between the floor and $z = 150$ mm. Here the moving floor shear stresses are smaller up to approximately $z = 50$ mm and larger between $z = 50$ and 150 mm.

Streamwise velocity profiles in plane $y = 0.35H$ are compared in Fig. 18. The differences between the stationary and the moving floor flow on the slanted surface

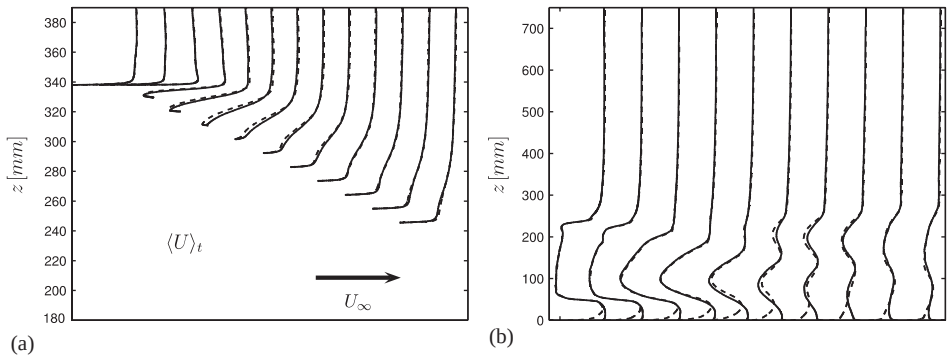

Fig. 18. Time-averaged $\langle U \rangle_t$ velocity profiles in plane $y = 0.35H$. (a) Slanted surface; (b) wake region. Moving floor (solid curve). Stationary floor (dashed curve).

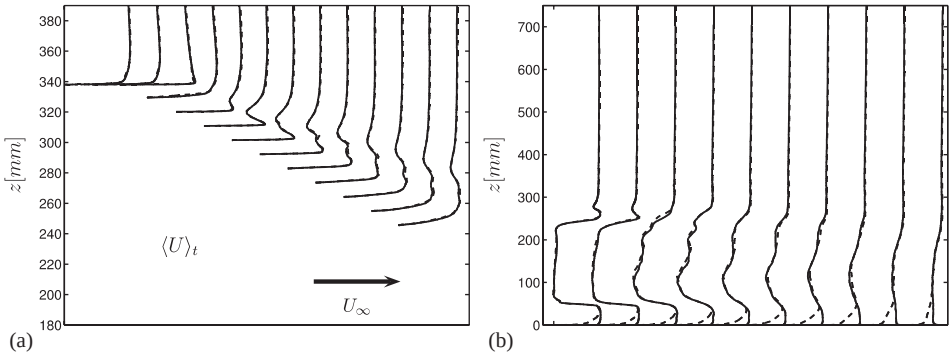

Fig. 19. Time-averaged $\langle U \rangle_t$ velocity profiles in plane $y = 0.63H$. (a) Slanted surface; (b) wake region. Moving floor (solid curve). Stationary floor (dashed curve).

are smaller here than in the symmetry plane (compare Figs. 18a and 16a). Differences in the wake (Fig. 18b) are similar to those found in the symmetry plane except for profiles $x = 0.826H$ and $x = H$ (the sixth and the seventh profiles from the left, respectively). Here we find a slightly larger magnitude of $\langle U \rangle_t$ for the moving floor case in the region between approximately $z = 150$ and 250 mm.

Fig. 19 shows a comparison of the $\langle U \rangle_t$ profiles in plane $y = 0.63H$. Differences between the streamwise velocities on the slanted surface (Fig. 19a) have now completely disappeared. This together with the observation of the decrease in differences in $\langle U \rangle_t$ profiles in plane $y = 0.35H$ as compared to the symmetry plane, $y = 0$, indicate that the flow on the slanted surface becomes independent of the motion of the floor as we move from the symmetry plane toward the lateral sides of the body. We have already seen in Fig. 13 that the cone-like vortices, $T_{\ell 3}$ and T_{r3}, are not affected by the change in the boundary condition of the floor. All this leads to the conclusion that the flow close to the lateral sharp edges, S_ℓ, is not affected by floor motion. This flow is dominated by strong cone-like vortices that are influenced

more by the geometry of the rear of the body and the angle of the slanted surface than by the floor. As expected, the streamwise velocities are larger in the wake close to the floor ($z < 50$ mm) when the floor is moving (see Fig. 19b). No other significant differences are found in the $\langle U \rangle_t$ profiles in the wake between the two cases. Very small differences are found in the $\langle V \rangle_t$, $\langle W \rangle_t$ and $\langle uu \rangle_t$ profiles between the two flows (not shown here) in plane $y = 0.63H$.

5. Conclusions and discussion

In the past, reproduction of the relative motion between the floor and the ground vehicle has been employed only for racing vehicles. These are characterized by small ground clearance, which makes the influence of the floor motions (especially on the lift) large. Simulation studies of road effects on the flows around passenger and commercial vehicles [7] showed that the influence of the motion of the floor on the aerodynamic forces and of the deposition of water and dirt on the vehicle can be significant despite the relatively large distance of the underbody from the floor.

In this paper we have studied the influence of floor motion on the flow around a simplified car with a typical fastback geometry. It is found that the mass flux underneath the vehicle in the moving floor case increases and decreases in the streamwise and the spanwise directions, respectively, compared to the stationary floor case. This results in an increase in the surface pressure on the underbody (see Fig. 12). Similar observations were made in previous experimental studies (see for example [19]). These changes in the surface pressure were not reserved for the underbody only but were observed on both the slanted and the vertical rear surfaces as well.

Drag is reduced by 8% as a consequence of the increased surface pressure on the rear slanted and vertical surfaces, which is identical to the value found by Bearman et al. [4] for the flow around a typical 1:3-scale car. The change in lift is 16% compared to the 30% found in [4] for a 1:3-scale car. These numbers change with ground clearance and when the underbody has rear upsweep (see [4,5]). Depending on the shape of the vehicle and the distance from the floor, the aerodynamic forces can either increase or decrease [4,5]. It is thus not possible to make any generalizations about the influnce of the floor motions on the aerodynamic forces.

Besides the mean values of the aerodynamic forces, the periodicity of the flow is found to be influenced by the motion of the floor. For example, more regular fluctuations were found in the lift and drag coefficients when the floor is moving.

Surprisingly, the largest differences in the flow structures and the velocity and stress profiles between the two flows were not found in the wake behind the body (except close to the ground) but rather on the slanted surface of the body. The changes in the wake structures were limited primarily to the region above the floor below the shear layer coming from the underbody of the vehicle. Bearman et al. [4] observed a similar wake insensitivity to floor motion.

Finally, we conclude that there are clear indications of the influence of the relative motion between the floor and the vehicle on the flow around the vehicle. However,

the quantitative changes are limited to the near-floor flow and the flow on the slanted rear surface. The changes in the aerodynamic forces are significant and should justify proper simulation of the moving floor boundary condition in wind tunnel experiments and numerical simulations.

Acknowledgements

This work was supported by the FLOMANIA project. The FLOMANIA (Flow Physics Modelling—An Integrated Approach) is a collaboration between Alenia, AEA, Bombardier, Dassault, EADS-CASA, EADS-Military Aircraft, EDF, NUMECA, DLR, FOI, IMFT, ONERA, Chalmers University, Imperial College, TU Berlin, UMIST and St. Petersburg State University. The project is funded by the European Union and administrated by the CEC, Research Directorate-General, Growth Programme, under Contract No. G4RD-CT2001-00613.

Computer time on the Linux cluster, provided by the NSC (National Supercomputer Center in Sweden), is gratefully acknowledged.

References

[1] R.H. Barnard, Road Vehicle Aerodynamic Design, An Introduction, first ed., Addison-Wesley Longman Limited, 1996, ISBN 0-582-24522-2.
[2] L. Larsson, L. Hammar, L.-U. Nilsson, A. Berndtsson, K. Knutson, H. Danielson, A study of ground simulation-correlation between wind tunnel and water-basin tests of a full-scale car, SAE Paper 890368, 1989.
[3] E. Mercker, J. Wiedemann, Comparison of different ground simulation techniques for use in automotive wind tunnels, SAE Paper 900321, 1990.
[4] P.W. Bearman, D.D. Beer, E. Hamidy, J.K. Harvey, The effect of a moving floor on wind-tunnel simulation of road vehicles, SAE Paper No. 880245, 1989.
[5] J.P. Howell, The influence of ground simulation on the aerodynamics of simple car shapes with an underfloor diffuser, in: Road Vehicle Aerodynamics Conference, RAeS, Loughborough, UK, July 18–19, 1994.
[6] S.R. Ahmed, G. Ramm, G. Faltin, Some salient features of the time averaged ground vehicle wake, SAE Paper 840300, 1984.
[7] T. Lajos, L. Preszler, L. Finta, Effect of moving ground simulation on the flow past bus models, J. Wind Eng. Ind. Aerodyn. 22 (1986) 271.
[8] S. Krajnović, Large eddy simulations for computing the flow around vehicles, Ph.D. Thesis, Department of Thermo and Fluid Dynamics, Chalmers University of Technology, Gothenburg, 2002.
[9] S. Krajnović, L. Davidson, Numerical study of the flow around the bus-shaped body, ASME: J. Fluids Eng. 125 (2003) 500.
[10] S. Krajnović, L. Davidson, Large-eddy simulation of the flow around simplified car model, in: SAE 2004 World Congress, SAE Paper 2004-01-0227, Detroit, Michigan, USA, 2004.
[11] S. Krajnović, L. Davidson, Large eddy simulation of the flow around an Ahmed body, in: 2004 ASME Heat Transfer/Fluids Engineering Summer Conference, Charlotte, North Carolina, USA, 2004.
[12] S. Krajnović, L. Davidson, Flow around a simplified car, part I: large eddy simulation, ASME: J. Fluids Eng., September 2005.
[13] S. Krajnović, L. Davidson, Flow around a simplified car, part II: understanding the flow, ASME: J. Fluids Eng., September 2005.

[14] J. Smagorinsky, General circulation experiments with the primitive equations, Mon. Weather Rev. 91 (3) (1963) 99.
[15] L. Davidson, B. Farhanieh, CALC-BFC: a finite-volume code employing collocated variable arrangement and cartesian velocity components for computation of fluid flow and heat transfer in complex three-dimensional geometries, Report 95/11, Department of Thermo and Fluid Dynamics, Chalmers University of Technology, Gothenburg, 1995.
[16] C. Rhie, W. Chow, Numerical study of the turbulent flow past an airfoil with trailing edge separation, AIAA J. 21 (11) (1983) 1525.
[17] H. Nilsson, L. Davidson, CALC-PVM: a parallel SIMPLEC multiblock solver for turbulent flow in complex domains, Internal report 98/12, Department of Thermo and Fluid Dynamics, Chalmers University of Technology, Gothenburg, 1998.
[18] H. Lienhart, S. Becker, Flow and turbulente structure in the wake of a simplified car model, SAE Paper 2003-01-0656, 2003.
[19] W.H. Hucho, L.J. Janssen, G. Schwarz, The wind tunnel's ground plane boundary layer—its interference with the flow underneath cars, SAE Paper No. 750066, 1975.